

Inverse Quantum Potential Reconstruction via Generalized Bertlmann–Martin Inequalities

M. Gage Plott

Department of Mathematics, University of Tennessee at Chattanooga, Chattanooga, TN 37403, USA
mgplott13@gmail.com

F. Ayça Çetinkaya

Department of Mathematics, University of Tennessee at Chattanooga, Chattanooga, TN 37403, USA

Rick Mukherjee

Department of Physics, University of Tennessee at Chattanooga, Chattanooga, TN 37403, USA

Reconstructing a 1D quantum potential, $V(r)$, from a few bound-state energies is a long-standing inverse problem. We present a Laplace-moment reconstruction pipeline that ties the Bertlmann–Martin gap bound to generalized Bertlmann–Martin (GBM) even-moment ladders, continues the Laplace image with Padé approximants, and inverts the transform to recover $\rho(r)$ and $V(r)$. Odd moments are supplied by a physically consistent interpolation scheme. The paper emphasizes mode ladders that isolate each approximation layer and a reproducibility spine that records benchmark settings and diagnostics. All numerical results are tied to archived configurations, and conclusions are reported empirically under the stated benchmark settings.

Keywords: Inverse quantum problems; Schrödinger equation; Radial potentials; Laplace transform; Generalized Bertlmann–Martin (GBM) inequalities; Padé approximants; Spectral theory; Moment problems; Numerical inverse Laplace methods.

Mathematics Subject Classification 2020: 34A55; 34L40; 81Q05; 44A10; 44A60; 41A21; 65R32

1. Introduction

The inverse spectral problem, broadly defined, seeks to reconstruct a potential function from partial or complete information about the spectral data of a differential operator. The greatest success in the inverse problem theory was achieved for the one-dimensional Schrödinger operator

$$\mathcal{L}y := -y'' + q(x)y. \tag{1.1}$$

where \mathcal{L} denotes the one-dimensional Schrödinger operator and $q(x)$ denotes the potential function.

Units and Conventions. Unless stated otherwise, we work in Hartree atomic units (a_0 , Hartree) with $\hbar = m_e = e = 4\pi\epsilon_0 = 1$, so the kinetic prefactor is $\hbar^2/(2m_e) = 1/2$. The one-dimensional Sturm–Liouville form $-y'' + q(x)y$ in (1.1) is the equivalent scaled form obtained after radial reduction and normalization choices. For reference, the full-constants form appears in (2.5) in Section 2.

The first result in this direction is due to Ambarzumian [1]. He showed that if the eigenvalues of the boundary value problem

$$-y'' + q(x)y = \lambda y, \quad y'(0) = y'(\pi) = 0 \quad (1.2)$$

are $\lambda_k = k^2$, $k \geq 0$, then $q = 0$. But this result is an exception from the rule, and in general the specification of the spectrum does not uniquely determine the operator (1.1). Afterwards Borg [2] proved that the potential is uniquely recovered from the two spectra corresponding to various pairs of boundary conditions and sharing the same boundary conditions at π , one of which should be Dirichlet boundary condition at 0. Levinson [3] extended Borg’s result by removing the restriction of Dirichlet boundary condition at 0. Tikhonov in [4] obtained the uniqueness theorem for the inverse problem on the half-line from the given Weyl function.

Over the past century, several inverse frameworks have emerged, each with different assumptions on available data and different tradeoffs in uniqueness, stability, and computational cost. In this paper, we use a transform-based ladder: Bertlmann–Martin (BM) links spectral gaps to moments, generalized Bertlmann–Martin (GBM) constrains the even-moment ladder, Padé continuation stabilizes the transform, and inversion recovers the density and potential. Fourier is discussed only for context; the benchmark results and figures in this RMP revision are Laplace-only. We also keep a reproducibility trail so each stage of the pipeline can be checked independently.

1.1. *Classical Approaches: Gel’fand–Levitan and Marchenko Theory*

One of the most celebrated and mathematically elegant approaches is based on integral equation methods developed by Gel’fand and Levitan [5], and independently by Marchenko [6]. They discovered that as a key to the solution of the inverse problem one can take the integral kernel of the transmutation operator. This requires solving the integral equation

$$K(x, t) + \int_0^x K(x, s)f(s, t)ds = f(x, t), \quad 0 \leq t \leq x \quad (1.3)$$

for the function $K(x, t)$ at each fixed $x \in [0, 1]$. Here the function $f(x, t)$ is obtained from data of the spectral function type. The potential is recovered from $q(x) = 2(d/dx)K(x, x)$. However, classical Gel’fand–Levitan–Marchenko (GLM) methods may not be available in physical or computational settings and thus may not be very fruitful for computational purposes as discussed in [7] where the authors said that the main difficulty with the method, and one that limits its effectiveness,

is the sensitivity of the solution of the integral equation on the data function $f(x, t)$ which is given as the difference of two series in which, although the combination converges, each component is rapidly divergent. This leads to difficulties in accurate computation of f . In addition, the method has a relatively high operational count and, at least in the usual formulation, is restricted to spectral data consisting of eigenvalues and norming constants. Despite the drawbacks, the approach has provided a starting place for other techniques (see for example [8,9,10,11,12]).

Broader context. Beyond the Gel'fand–Levitan and Marchenko integral-equation frameworks, the classical inverse-scattering literature provides comprehensive treatments of phase shifts, S -matrices, and fixed-energy formulations [13,14]. Complementary to these are optimization-based schemes that cast the inverse problem as a minimization over admissible potentials or parameters [15]. In parallel, bound-state-driven approaches reconstruct ground-state information from moments generated by transforms of the reduced radial density, including Fourier- or Laplace-based pipelines [16,17]. Our work situates itself in the latter class, combining generalized Bertlmann–Martin (GBM) inequalities with a Laplace-moment representation and a Padé continuation/inversion stage [18,17].

Remark 1.1 (Even and odd moments outside GBM). Transform generators produce ground-state moments as Taylor coefficients at the origin. Writing $\widehat{\rho}(k)$ for the Fourier transform and $L(q)$ for the Laplace image of the reduced radial density,

$$\widehat{\rho}(k) = \sum_{n \geq 0} \frac{(ik)^n}{n!} \langle r^n \rangle, \quad L(q) = \sum_{n \geq 0} \frac{(-1)^n}{n!} \langle r^n \rangle q^n,$$

both parities appear directly as series coefficients. Practical schemes continue these series rationally (Padé) before inversion [16,17]. By contrast, GLM/Marchenko-type pipelines recover V or the radial ground-state wavefunction $R_{0,0}$ from scattering/spectral data first, with moments then computed *a posteriori* via $\langle r^n \rangle = \int_0^\infty r^{n+2} |R_{0,0}(r)|^2 dr$ [13,14]. Independent sum-rule or virial identities can supplement constraints across parities in specific model classes.

1.2. Inverse Scattering Techniques

While the Gel'fand–Levitan and Marchenko approaches rely on spectral functions or norming constants, a closely related line of work focuses more directly on scattering data itself. These inverse scattering techniques offer an alternative route to potential reconstruction that is often more directly tied to physical observables.

The GLM methods constitute a class of integral equation approaches to the inverse spectral and scattering problems. These methods are capable of incorporating scattering data—particularly in the Marchenko formulation, which reconstructs the potential from the reflection coefficient and discrete bound-state information. In this sense, the GLM framework is subsumed within the broader domain of inverse scattering theory.

However, inverse scattering techniques as a whole encompass a wider range of methods that may or may not employ the GLM formalism. For instance, phase-shift inversion methods and other direct approaches often reconstruct the potential without resorting to the integral equations characteristic of the GLM framework. These alternative methods may rely instead on asymptotic analysis, variational techniques, or numerical fitting procedures. In [15], various optimization-based methods for inverse scattering problems are presented, emphasizing that analytical inversion procedures are often unavailable, thereby requiring parameter-fitting techniques. The inverse scattering problem is reformulated as an optimization problem and solved using algorithms such as the Hybrid Stochastic-Deterministic minimization algorithm. These methods do not rely on the integral equations characteristic of the GLM framework but instead employ numerical fitting procedures to reconstruct the potential from scattering data.

Thus, while GLM-based approaches are central to the mathematical theory of inverse scattering, it is important to note that *all GLM-based methods may be viewed as part of inverse scattering theory, but not all inverse scattering techniques rely on the GLM formalism*. This distinction underscores the methodological diversity within inverse problems in quantum mechanics and reflects the different types of data—spectral functions, norming constants, or scattering observables—that each approach is designed to accommodate.

1.3. Moment-Based Reconstruction Method

The moment-based reconstruction method offers several significant advantages over both the GLM integral equation framework and conventional inverse scattering techniques, particularly in the context of bound-state quantum systems.

Unlike the GLM method, which typically requires the complete spectral function (including norming constants or reflection coefficients) to formulate and solve an integral equation [13,14], the moment-based approach requires only a finite set of discrete eigenvalues—specifically, the lowest bound-state energy for each angular momentum quantum number. This significantly lowers the data burden and makes the method more applicable to physical systems where only limited spectral data are experimentally accessible, such as nuclear or atomic systems with confined geometries.

Similarly, inverse scattering methods rely on detailed scattering phase shifts or full S-matrix data across a continuous energy range [14], which are often difficult to obtain with high precision. In contrast, the moment-based reconstruction method circumvents the need for such data, relying instead on measurable low-lying bound-state energies, thereby enhancing practical feasibility.

The GLM and inverse scattering frameworks are known to be sensitive to data perturbations, particularly when applied numerically. Ill-posedness and instability are common concerns, especially when dealing with incomplete or noisy data [15]. The moment-based method, by contrast, converts the inverse problem into a recur-

sive moment-generation process that is numerically stable and convergent under a wide range of conditions. The use of Padé approximants for analytic continuation of the density’s Fourier transform, as demonstrated in [16], or the density’s Laplace transform, as demonstrated in [17], provide a reliable and controlled extension beyond the radius of convergence of the power series, avoiding the divergence problems typical of truncated expansions. Moreover, the method allows for systematic refinement through iterative improvement of the moment-to-spectrum correspondence, enabling increasingly accurate reconstructions without sacrificing generality.

Why GBM + Laplace. (i) **Theory anchor:** GBM inequalities furnish rigorous, potential-agnostic upper bounds on even ground-state moments (equivalently, upper bounds on low-lying gaps after rearrangement) [18]. (ii) **Data efficiency:** Unlike GLM/Marchenko, which typically require extensive phase shifts or spectral functions [13,14], a compact low-lying subset seeds an even-moment ladder; odd moments are supplied within the transform/Padé stage [17]. (iii) **Stability:** Working with $L(q)$ and rational continuation (with simple pole-filtering/averaging) mitigates ill-conditioning from finite-moment truncations before inversion [17]. (iv) **Actionable for labs:** The pipeline maps a compact set of measured lines to constrained moment bands (via GBM), with tunable Padé order/filters and straightforward uncertainty propagation.

1.4. A Case for Bertlmann–Martin Inequalities as Meaningful Ansätze

The corrected, generalized Bertlmann–Martin inequalities (GBMs) provide a practical ansatz for Laplace-transform-based inverse spectral methods. They establish recurrences between ground-state moments and bound-state energies. With an additional correction factor to *saturate* the GBM bounds (exact for the harmonic oscillator (HO) and Coulomb), the method yields accurate moment estimates beyond those exactly solvable cases. In the Laplace pipeline, both even and odd moments enter a Padé-approximated transform, which is then inverted to recover density and potential.

Across the benchmarks in §3, this framework reproduces the ground-state density and potential accurately from compact spectral input. In Coulomb, Hulthén, and Kratzer, low Padé orders (for example $P(0,3)$ or $P(0,4)$) already track the exact behavior well, while the Fourier-based route may require substantially higher order (e.g., Kratzer $P(6,10)$) for comparable quality [16]. Even for the hyperbolic molecular well, low orders such as $P(0,4)$ – $P(0,5)$ remain close to the exact transform and produce usable potential reconstructions. The same GBM structure has also been extended to complex potentials with real spectra, which supports its broader applicability beyond strictly Hermitian testbeds.

One practical advantage of the Laplace-formulated GBM method is lower spectral-data demand than many classical inverse workflows. In principle, GLM-

type methods require near-complete spectral information (or full scattering data) for uniqueness, and Fourier moment pipelines can need much deeper input sequences. In the benchmark protocol used here, the GBM–Laplace path uses a compact recurrence-consumed subset (7 inputs for Coulomb; 22 total for non-Coulomb cases), and reconstruction quality is validated empirically with reported diagnostics and error metrics. The least-squares (LSQ) baseline remains an important comparator, but LSQ-versus-Laplace ranking in this manuscript is treated as an empirical result under the stated benchmark configuration, not as a universal method claim. A concise listing of current numerical inverse methods can be found in Vladislav V. Kravchenko’s paper [19].

In what follows, we present the GBM-derived even-moment ladder, our Laplace representation and Padé continuation strategy, and the stable inversion procedure, with benchmarks on Coulomb, harmonic oscillator, Kratzer, Hulthén, and hyperbolic molecular well potentials.

2. Methodology: The Inverse Laplace Method Using GBMs

2.1. Preliminaries and notation

We denote the ground-state radial wave by $R_{0,0}(r)$, the reduced radial wavefunction by

$$\chi_{0,0}(r) := r R_{0,0}(r),$$

and the radial density by

$$\rho_{0,0}(r) := |R_{0,0}(r)|^2, \quad r \geq 0, \quad (2.1)$$

so that $\int_0^\infty r^2 \rho_{0,0}(r) dr = 1$. Ground-state moments are

$$\langle r^n \rangle_{0,0} := \int_0^\infty r^{n+2} \rho_{0,0}(r) dr, \quad n = 0, 1, 2, \dots, \quad (2.2)$$

and the *Laplace transform* of $r^2 \rho_{0,0}(r)$ is

$$L(q) := \int_0^\infty e^{-qr} r^2 \rho_{0,0}(r) dr, \quad q \geq 0, \quad (2.3)$$

with Maclaurin expansion

$$L(q) = \sum_{n \geq 0} \frac{(-1)^n}{n!} \langle r^n \rangle_{0,0} q^n. \quad (2.4)$$

These conventions match the Hartree atomic-units basis declared in Section 1. Where a source-derived block uses the scaled form $\hbar = 2m = 1$, we interpret it as an algebraically equivalent rescaling of the same equation family in (2.5). We consider the non-relativistic Schrödinger equation in 3D with spherical symmetry for a local, central potential $V(r)$

$$\left[-\frac{\hbar^2}{2m} \nabla^2 + V(\mathbf{r}) \right] \Psi(\mathbf{r}) = E \Psi(\mathbf{r}). \quad (2.5)$$

Notation and units conventions State labels use radial-orbital indices (n_r, ℓ) throughout. For the lowest channels used in this manuscript, $(n_r, \ell) = (0, 0), (0, 1), (1, 0), (0, 2)$. When both symbols appear, $E_{0, \ell}$ denotes the yrast level in the ℓ -channel ($n_r = 0$), while $E_{\ell, 0}$ denotes the ℓ -th radial excitation in the $\ell = 0$ channel used in $f(\ell)$. Moments of the ground-state density are

$$\langle r^k \rangle_{0,0} = \int_0^\infty \rho_{0,0}(r) r^{k+2} dr = \int_0^\infty |R_{0,0}(r)|^2 r^{k+2} dr. \quad (2.6)$$

This manuscript is anchored to Hartree atomic units (a_0 , Hartree), matching the code stack and dissertation chapters. See Appendix A for derivations of the equations that follow, especially the change of variables required to go from 3D to 1D (Theorem 1).

Step 1: Even Moments from Generalized Bertlmann–Martin Inequalities (GBMs)

Starting from sum rules with the operator $Q_{\ell,0}(\mathbf{r}) = r^\ell Y_{\ell 0}(\theta, \phi)$, one has

$$(E_{0,\ell} - E_{0,0}) \sum_{n_r} |\langle 0,0 | Q_{\ell,0} | n_r, \ell \rangle|^2 \leq \sum_{n_r} (E_{n_r,\ell} - E_{0,0}) |\langle 0,0 | Q_{\ell,0} | n_r, \ell \rangle|^2, \quad (2.7)$$

which leads to an even-moment upper bound (for $\ell \geq 1$; equivalently an upper bound on the gap when rearranged)

$$\boxed{\langle r^{2\ell} \rangle_{0,0} \leq \frac{\ell(2\ell+1)}{E_{0,\ell} - E_{0,0}} \langle r^{2\ell-2} \rangle_{0,0}}. \quad (2.8)$$

$$E_{0,\ell} - E_{0,0} \leq \frac{\ell(2\ell+1) \langle r^{2\ell-2} \rangle_{0,0}}{\langle r^{2\ell} \rangle_{0,0}}. \quad (2.9)$$

Saturating factor. BM relations give upper bounds on moments (equivalently, upper bounds on gaps after rearrangement). To approximate saturation, introduce a correction factor on the RHS:

$$f(\ell) = 1 - \frac{\ell}{2(\ell+1)} \left[\frac{E_{\ell,0} + E_{0,0} - 2E_{0,\ell}}{E_{\ell,0} - E_{0,0}} \right]^2, \quad (2.10)$$

which is exact for the harmonic oscillator and Coulomb potentials and serves as a good ansatz otherwise (refined iteratively if desired).

Cross-references: Eq. (2.8), (2.10).

Step 2: From Moments to the Laplace Transform $L(q)$

Define the Laplace transform of the reduced density $\chi_{0,0}^2(r) = r^2 \rho_{0,0}(r)$:

$$L(q) = \int_0^\infty r^2 \rho_{0,0}(r) e^{-qr} dr. \quad (2.11)$$

Expanding $e^{-qr} = \sum_{n=0}^{\infty} (-1)^n q^n r^n / n!$ and interchanging sum and integral yields the power series

$$L(q) = \sum_{n=0}^{\infty} \frac{(-1)^n}{n!} \langle r^n \rangle_{0,0} q^n. \quad (2.12)$$

Key point. The Laplace transform needs *both* parities of moments. Even moments come from Step 1 (with the saturation factor if used); *odd* moments are not fixed by BM and must be supplied by an appropriate interpolation/completion of the moment sequence [17]. In this manuscript, one declared odd-moment method family is used per run (monotone interpolation, constrained low-order fit, or maximum-entropy closure), and the choice is recorded in reproducibility metadata.

Analytic continuation in q with Padé. The series (2.12) has a finite radius of convergence. $L(q)$ is continued beyond q_{\max} by replacing the truncated series with a Padé rational approximant $P(N, D)$. In practice, one constructs several (N, D) and (i) discards those with obstructive singularities and (ii) averages over the acceptable fractions to reduce dispersion at large q .

Inverse Laplace transform (Bromwich integral). Once $L(q)$ is represented by a Padé $P(N, D)$, we invert by the Bromwich integral

$$\chi_{0,0}^2(r) = r^2 \rho_{0,0}(r) = \frac{1}{2\pi i} \int_{c-i\infty}^{c+i\infty} e^{qr} L(q) dq, \quad c > \Re(\text{all singularities}). \quad (2.13)$$

For simple rational forms, the contour integral can be done analytically (residues). In general, one performs a suitable numerical inversion; different algorithms exist, and efficacy can vary with each potential. Numerical tests are currently underway. *Cross-references:* Eq. (2.12).

Step 3: Recovering $\chi_{0,0}$ and $R_{0,0}$

Having obtained $\chi_{0,0}^2(r)$ from (2.13), we take the positive square root to get the reduced wavefunction $\chi_{0,0}(r)$, and hence the radial ground state

$$R_{0,0}(r) = \frac{\chi_{0,0}(r)}{r}, \quad r > 0. \quad (2.14)$$

(At very small r , numerical inversion may be sensitive. Interpolation techniques can be used locally when necessary.)

Cross-references: Eq. (2.13).

Step 4: Inverting Schrödinger to Obtain the Potential $V(r)$

For the $\ell = 0$ ground state (Hartree a.u.; equivalently under an $\hbar = 2m = 1$ rescaling), recover the potential from the reduced wavefunction by

$$V(r) = E_{0,0} + \frac{\chi''_{0,0}(r)}{\chi_{0,0}(r)}, \quad r > 0. \quad (2.15)$$

For stability near $r = 0$, use $\langle r^{-1} \rangle$ and $\langle r^{-2} \rangle$ from $L(q)$ to constrain $\rho(0)$ (Stieltjes approach) [20].

3. Benchmark Results**1D Simulations**

This section reports benchmark results for Coulomb, harmonic oscillator, Hulthén, Kratzer, and a canonical hyperbolic molecular well to evaluate the Laplace inverse method built on GBM inequalities. The five benchmark-sheet figures are Laplace diagnostics only; Fourier results are intentionally out of scope in this revision. We compare against the variational least-squares baseline of Roehrl [21] [22] [23] under a shared benchmark configuration. For cross-potential comparability, LSQ settings are calibrated on Coulomb and then transferred unchanged to the remaining potentials. Each sheet has four panels: top-left $V(r)$, top-right $r^2\rho_{0,0}(r)$, bottom-left $L(q)$, and bottom-right $\chi_{0,0}(r)$, each shown as reconstructed versus exact.

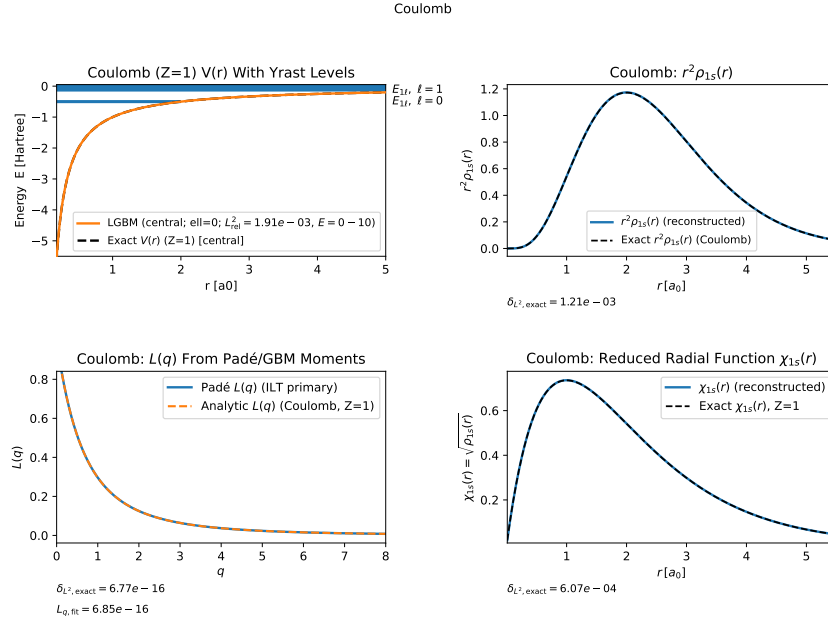


Fig. 1. Coulomb benchmark sheet ($Z = 1$): reconstructed versus exact $V(r)$, $r^2 \rho_{0,0}(r)$, $L(q)$, and $\chi_{0,0}(r)$.

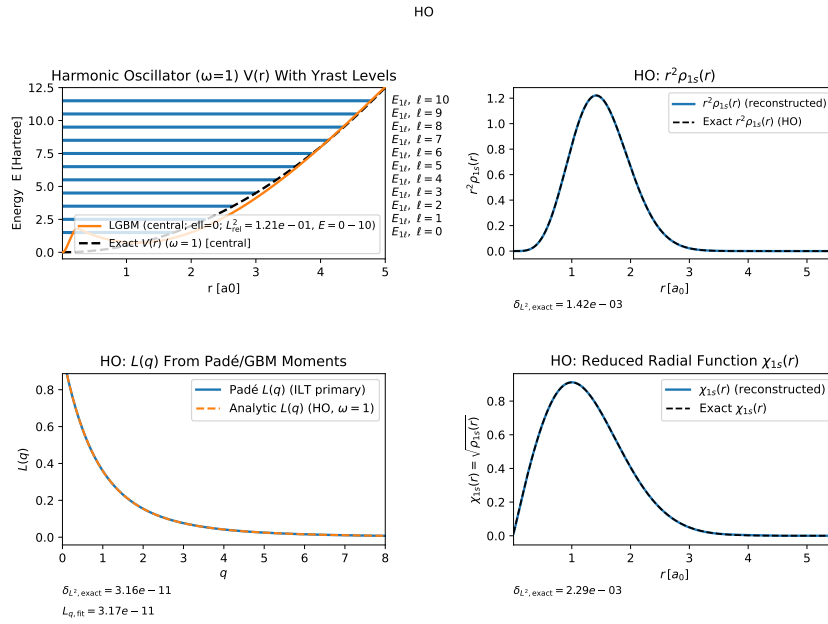


Fig. 2. Harmonic oscillator benchmark sheet ($\omega = 1$): reconstructed versus exact $V(r)$, $r^2 \rho_{0,0}(r)$, $L(q)$, and $\chi_{0,0}(r)$.

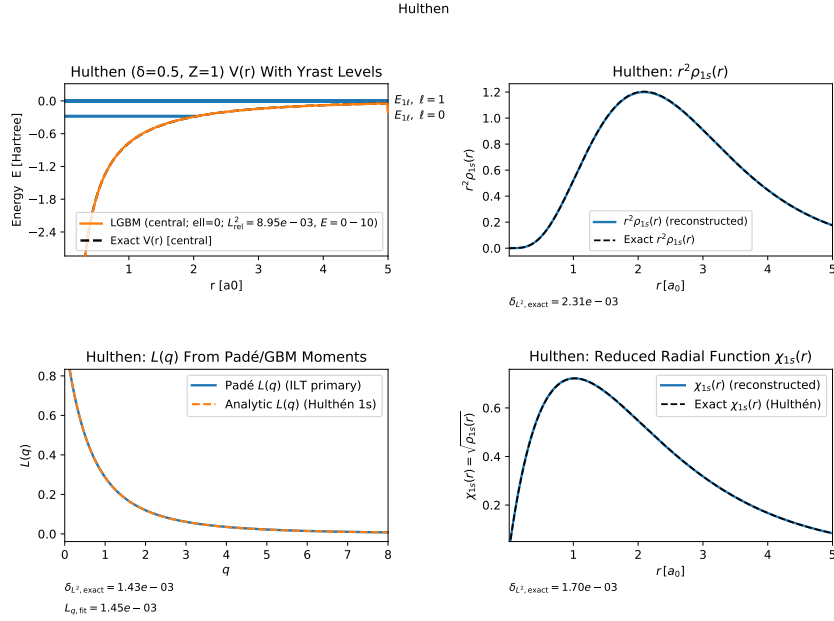


Fig. 3. Hulthén benchmark sheet ($V_0 = \lambda = 0.5$): reconstructed versus exact $V(r)$, $r^2 \rho_{0,0}(r)$, $L(q)$, and $\chi_{0,0}(r)$.

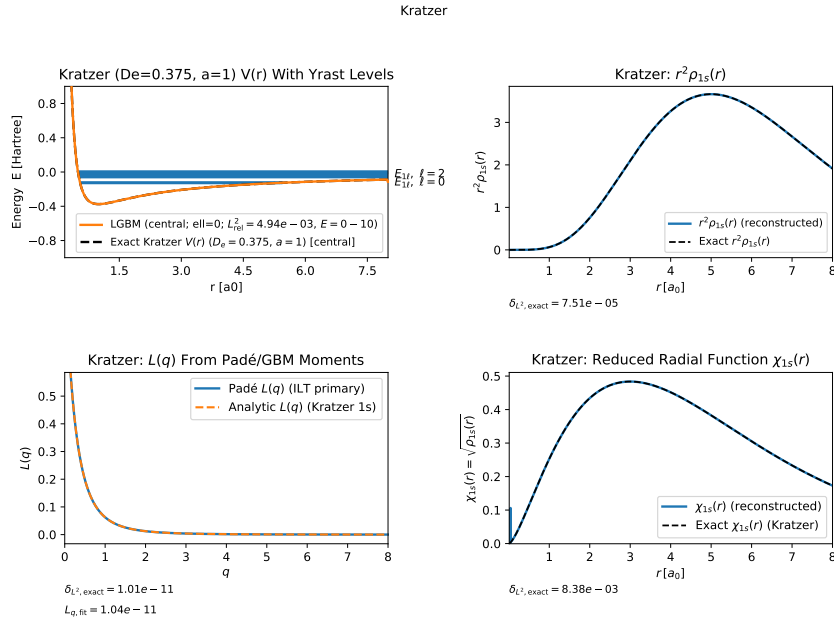


Fig. 4. Kratzer benchmark sheet ($B = \frac{3}{8}, a = 1$): reconstructed versus exact $V(r)$, $r^2 \rho_{0,0}(r)$, $L(q)$, and $\chi_{0,0}(r)$.

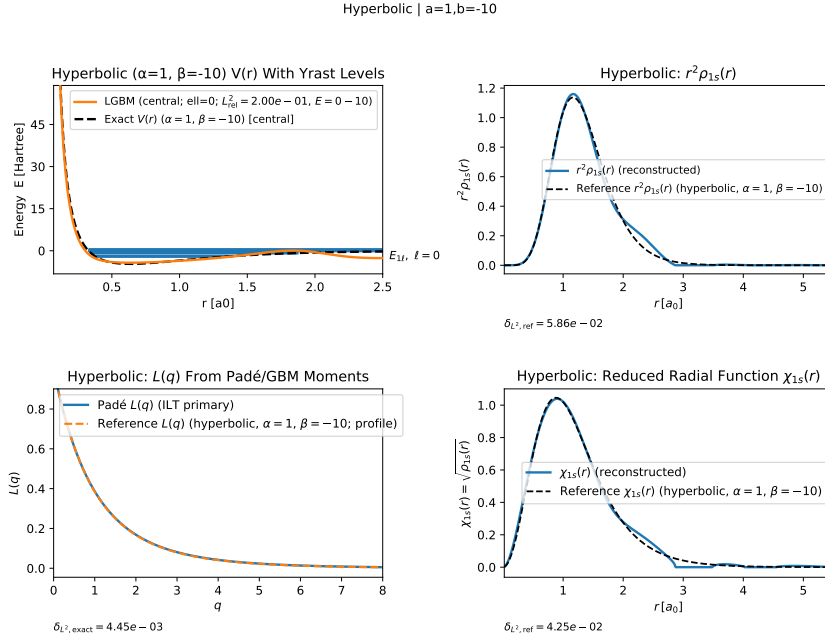


Fig. 5. Hyperbolic molecular well benchmark sheet (canonical $A_{\text{sinh}} = 1, B_{\text{cosh}} = -10, \alpha = \beta = 1$): reconstructed versus exact $V(r), r^2 \rho_{0,0}(r), L(q)$, and $\chi_{0,0}(r)$.

Method-comparison overlays ($V(r)$ only). The next five figures provide two-panel comparisons for each benchmark: the left panel overlays Exact, Laplace (GBM), and LSQ $V(r)$, and the right panel reports pointwise absolute error. The LSQ baseline uses 60 DD + 60 DN eigenvalue constraints (120 total), with fixed optimization settings shared across potentials in this benchmark configuration.

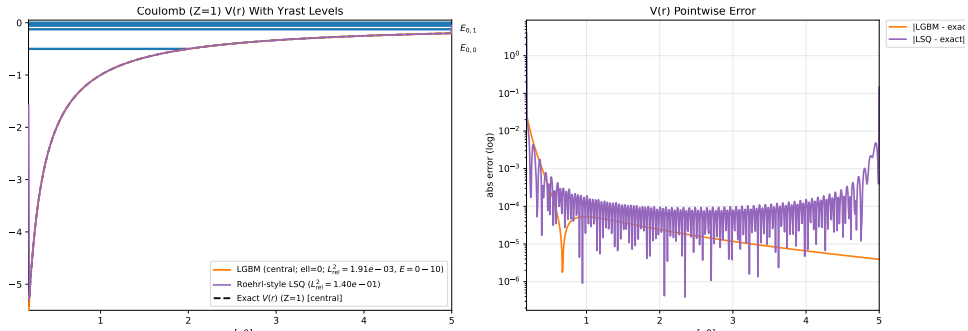


Fig. 6. Coulomb two-panel comparison ($Z = 1$): left $V(r)$ overlay (Exact, Laplace (GBM), LSQ); right pointwise absolute error.

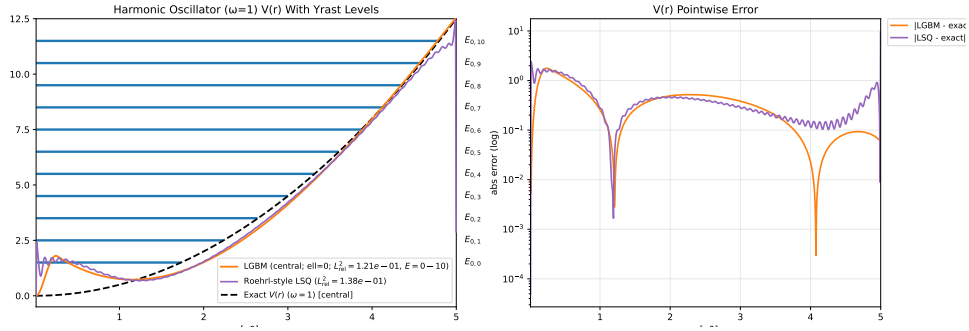


Fig. 7. Harmonic oscillator two-panel comparison ($\omega = 1$): left $V(r)$ overlay (Exact, Laplace (GBM), LSQ); right pointwise absolute error.

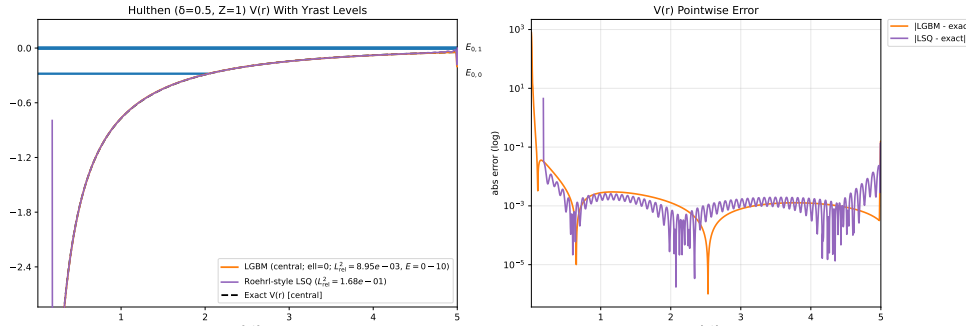


Fig. 8. Hulthén two-panel comparison ($V_0 = \lambda = 0.5$): left $V(r)$ overlay (Exact, Laplace (GBM), LSQ); right pointwise absolute error.

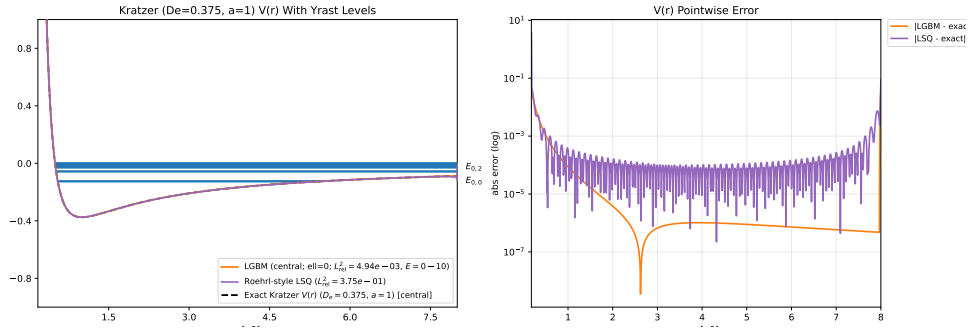


Fig. 9. Kratzer two-panel comparison ($B = \frac{3}{8}, a = 1$): left $V(r)$ overlay (Exact, Laplace (GBM), LSQ); right pointwise absolute error.

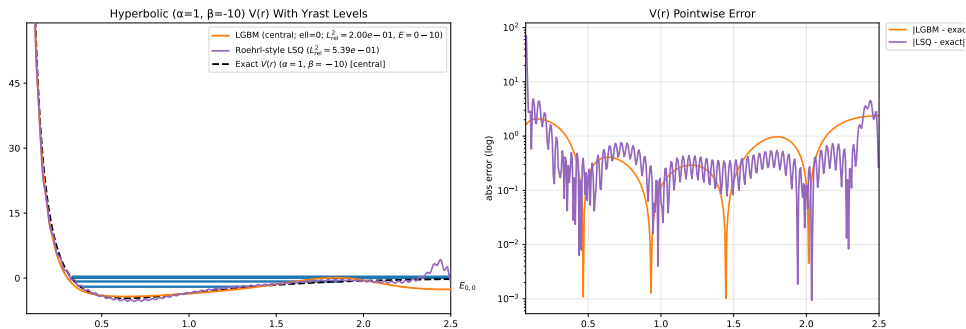


Fig. 10. Hyperbolic molecular well two-panel comparison (canonical case $A_{\sinh} = 1$, $B_{\cosh} = -10$, $\alpha = \beta = 1$): left $V(r)$ overlay (Exact, Laplace (GBM), LSQ); right pointwise absolute error.

Table 1. Relative L^2 values on five 1D benchmarks for Laplace (GBM) and LSQ. LSQ entries use 120 total constraints (60 DD + 60 DN), with `num_pairs=60` per boundary set.

Potential	LSQ (rel. L^2)	LGBM (rel. L^2)
Coulomb	1.40e-1	1.91e-3
HO	1.38e-1	1.21e-1
Hulthén	1.68e-1	8.95e-3
Kratzer	3.75e-1	4.94e-3
Hyperbolic molecular well	5.39e-1	2.00e-1
Hyperbolic variant (draft)	–	3.11e-3
Hyperbolic intermediate (draft)	–	7.29e-3

Note. Canonical five rows use the validated Laplace baseline with LSQ comparator and match the same $V_{L^2, \text{rel}}$ metric reported in the canonical LSQ overlay figure legends. Hyperbolic variant/intermediate rows are draft/non-validated extension entries and currently reflect promoted fallback Laplace modes (HYV ‘p6-analytic_pade’, HYI ‘p6-hybrid1’) pending extension ‘p6-gbm’ promotion; LSQ extension values remain pending validated provenance backfill.

Interpretation policy for LSQ vs Laplace. Method ranking is taken directly from the reported benchmark metrics (here, relative L^2 on $V(r)$); no method is assumed dominant a priori. The Roehrl-style LSQ baseline is treated as an implementation-configured comparator with 60 DD + 60 DN eigenvalue constraints (120 total). Coulomb and the remaining potentials are compared under this shared benchmark basis, so conclusions are empirical for the stated settings rather than method-universal claims.

GBM level-accounting note. For the canonical benchmark runs in this paper, `levels_spec=0-120` is a selection/load scope and is not the GBM recurrence-consumed ladder size. The recurrence-consumed subset is tracked by `len(gbm_even.e11_used)` and, for benchmark-count comparisons, is compared against the LSQ 120-constraint basis:

- Coulomb: $\ell = 0, \dots, 6$, 7 recurrence-consumed inputs (`moment_max_order=12`); versus LSQ 120 this is 94.2% fewer.
- Non-Coulomb (HO, Hulthén, Kratzer, hyperbolic canonical): $\ell = 0, \dots, 10$, 22 recurrence-consumed inputs total (11 yrast + 11 non-degenerate s -channel terms; `moment_max_order=20`); versus LSQ 120 this is 81.7% fewer.

Coulomb uses a degeneracy-based recurrence path; the non-Coulomb benchmarks use yrast plus contiguous s -channel ladder selection. The plotted “levels=11” annotation on $V(r)$ panels is a display setting and is not the GBM recurrence-consumed ladder count.

Reproducibility note. All figures and tables in this draft are generated from archived benchmark runs with recorded settings and checksums; the detailed provenance record is maintained in companion repository documentation.

4. Discussion and practical considerations

We interpret the 1D ground-state benchmarks of Section 3 and summarize practical guidance for deploying the pipeline steps (GBM moment ladder, Laplace representation, Padé continuation, inverse Laplace, and density-to-potential mapping). Our goal is to make the method reliable across potentials with qualitatively different spectra (Coulomb, HO, Kratzer, Hulthén, hyperbolic molecular well).

4.1. Inputs, scaling, and noise

The pipeline assumes (i) a consistent atomic-units convention (with any $\hbar = 2m = 1$ source form treated as an equivalent rescaling), (ii) a set of low-lying gaps $\{\Delta_\ell\}_{\ell \geq 1}$ measured against the $\ell = 0$ ground state, and (iii) a small set of even moments or, equivalently, a truncated series for the Laplace transform $L(q)$ of $r^2\rho(r)$. When gaps or moments are empirical, pre-whitening (centering/rescaling) and simple outlier checks prevent single entries from dominating Padé selection. If gaps carry uncertainty, propagate it by bootstrapping the gaps, re-running the ladder/Padé steps, and reporting dispersion of the recovered ρ (we refrain from full uncertainty quantification here, but the averaging in the Padé averaging step reduces variance).

4.2. Moment ladder depth and stability

The GBM ladder inequality supplies upper bounds on even moments (equivalently, upper bounds on gaps after rearrangement), which stabilizes the truncated series for $L(q)$. In practice, a shallow ladder (four–six even moments) is often sufficient; deeper ladders help only if the gaps are accurate. Two simple diagnostics are useful: (a) *consistency*—successive GBM steps should not amplify small numerical noise into alternating-sign moment estimates; (b) *sensitivity*—dropping the topmost step should not drastically change the near-diagonal Padé choice.

4.3. Padé continuation: admissible sets and filters

Empirically, near-diagonal Padé indices with $|M - N| \leq 1$ balance bias and variance. We *discard* any candidate $[M/N]_L$ with obstructive poles in the closed right half-plane (the obstructive-pole filter criterion), then average the survivors (the Padé model average). This “model-averaging” stabilizes the continuation when the truncated series carries modest noise and mitigates occasional spurious pole-zero cancellations. As a rule of thumb, widening the admissible set (more near-diagonal pairs) helps only if the obstructive-pole filter remains strict.

4.4. Inverse Laplace in practice

When $\bar{L}(q)$ is rational with simple poles, the analytic inverse (residues) yields a compact exponential sum in the partial-fraction inverse representation that is fast and interpretable. Otherwise, a numerical Bromwich inversion is a robust fallback. In that case, choose a scheme with error control and proven convergence accelerations (e.g., de Hoog–Knight–Stokes’ Fourier-series acceleration or Abate–Whitt variants); moderate oversampling in the complex plane typically improves stability for 1D radial densities.^a

4.5. From density to potential: grids and regularization

To obtain $V(r) = E_0 + u_0''(r)/u_0(r)$ from $u_0(r) = r\sqrt{\rho(r)}$, use a monotone r -grid with spacing small enough to resolve the shortest exponential scale from the pole set. Compute derivatives with a smoothing differentiator (e.g., a low-order Savitzky–Golay stencil) to suppress high-frequency numerical noise without biasing near $r = 0$. Enforce the correct small- r behavior ($u_0(r) \sim a_0 + \mathcal{O}(r^2)$ for $\ell = 0$ channels) by either extrapolating u_0 or fitting a local polynomial consistent with regularity.

4.6. Defaults that worked across the five benchmarks

On Coulomb and HO, very low Padé orders already reproduce $L(q)$ accurately; on Hulthén, Kratzer, and the hyperbolic molecular well, a small family of near-diagonal fractions (e.g., total order $K \in [6, 10]$) with strict obstructive-pole filtering and simple averaging gave the best bias–variance tradeoff. For numerical inversion, analytic residues are preferred whenever \bar{L} is rational and well-conditioned; otherwise, a de Hoog/Abate–Whitt fallback with moderate truncation parameters suffices. Throughout, keep the analysis strictly 1D (no references to 2D/3D or sensitivity-study variants).

^aSee, e.g., de Hoog–Knight–Stokes (SIAM J. Sci. Stat. Comput., 1982) and Abate–Whitt overviews for practical Laplace inversions.

4.7. Limitations and failure modes

The method can stumble when (i) the truncated series is too shallow to identify stable near-diagonal Padé families, (ii) gaps are severely mis-estimated, or (iii) the true $L(q)$ has structure (e.g., branch cuts close to the origin) that mimics obstructive poles. In such cases, tightening the pole filter and shrinking the admissible index set often restores stability; if not, collect one or two additional reliable moments or refine the gap estimates.

4.8. Reproducibility and reporting

Report: unit conventions; the set of gaps; ladder depth; admissible Padé pairs and the filter rule; whether inversion was analytic or numerical (and any numerical parameters); and the grid and differentiator used for u_0''/u_0 . This suffices for exact reproduction and facilitates fair comparisons to least-squares baselines on future 1D testbeds.

5. Conclusion and outlook

We presented a compact pipeline for reconstructing 1D ground-state structure from minimal spectral information: (i) a GBM-constrained even-moment ladder seeded by low-lying gaps, (ii) a Laplace representation $L(q)$ of $r^2\rho(r)$ with truncated series, (iii) near-diagonal Padé continuation with an obstructive-pole filter and model averaging, and (iv) analytic (residue) or numerical inverse Laplace to recover ρ without overfitting. On five benchmarks (Coulomb, HO, Kratzer, Hulthén, hyperbolic molecular well), we report Laplace baseline values and LSQ comparison values under a shared benchmark basis (LSQ: 120 total constraints, 60 DD + 60 DN), and GBM count comparisons use the recurrence-consumed subset (7 for Coulomb, 22 for non-Coulomb cases). Comparative LSQ-vs-Laplace conclusions are therefore empirical for the stated settings rather than method-universal claims.

Appendix

Appendix A

A.1. Conditions on Some Potentials

All appendices of A refer to [18]. Some of the results below are valid for completely arbitrary potentials. However, most of the time, the authors restrict themselves to potentials that satisfy conditions (A)-(C). The harmonic oscillator and Coulomb potentials saturate the inequalities in Theorems 2 & 3. This appendix presents theorem statements and derivation labels directly in radial-orbital notation (n_r, ℓ) throughout.

$$\left(\frac{d}{dr}\right)^3 r^2 V \geq 0, \quad \lim_{r \rightarrow 0} r \left[V + \frac{1}{2} r \frac{dV}{dr} \right] \leq 0. \quad \text{A}$$

$$\frac{d}{dr} \frac{1}{r} \frac{d}{dr} \left[V(r) + \frac{1}{2} r \frac{dV}{dr} \right] < 0. \quad \text{B}$$

$$V'' < 0, \quad \text{i.e., } V \text{ is concave.} \quad \text{C}$$

Theorem Appendix A.1.

$$\langle r^2 \rangle_{0,0} < \langle r^2 \rangle_{0,1} < \langle r^2 \rangle_{1,0}. \quad (\text{Appendix A.1})$$

The left-hand inequality holds for any potential, while the right-hand inequality holds if conditions (A) and (B) are satisfied.

Remark Appendix A.1. Not all potentials with $E_{0,1} < E_{1,0}$ (implied by condition (A)) have $\langle r^2 \rangle_{0,1} < \langle r^2 \rangle_{1,0}$. A counterexample is the infinite square well, in which the (0,1)-channel repulsion from the origin dominates.

Remark Appendix A.2. The authors believe that $\langle r^2 \rangle_{0,0} < \langle r^2 \rangle_{1,0}$ should hold for any monotonous increasing potential, including the square well, but they have not succeeded in showing this. They find conditions in their appendix for which this is true, which contain, in particular, all attractive power potentials up to r^3 .

Proof. (Left-Hand Side)

$$\langle r^2 \rangle_{0,0} = \int_{\mathbb{R}^3} r^2 |\psi_{0,0}(\vec{r})|^2 d^3r.$$

Using spherical coordinates, where $r = \sqrt{x^2 + y^2 + z^2}$ and $d^3r = r^2 \sin \theta dr d\theta d\phi$,

$$\langle r^2 \rangle_{0,0} = \int_{\phi=0}^{2\pi} \int_{\theta=0}^{\pi} \int_{r=0}^{\infty} r^2 |\psi_{0,0}(r, \theta, \phi)|^2 r^2 \sin \theta dr d\theta d\phi.$$

Separating radial and angular components using $\psi_{0,0}(r, \theta, \phi) = R_{0,0}(r) Y_{\ell m}(\theta, \phi)$, with $\ell = m = 0$ for the (0,0) state gives

$$\langle r^2 \rangle_{0,0} = \int_0^{\infty} r^4 |R_{0,0}(r)|^2 dr \int_{\phi=0}^{2\pi} \int_{\theta=0}^{\pi} |Y_{00}(\theta, \phi)|^2 \sin \theta d\theta d\phi.$$

Looking at the angular component and considering the normalization condition, we have

$$\int_{\phi=0}^{2\pi} \int_{\theta=0}^{\pi} |Y_{00}(\theta, \phi)|^2 \sin \theta d\theta d\phi = 1, \quad \text{where } |Y_{00}(\theta, \phi)|^2 \text{ is constant.}$$

$\Rightarrow |Y_{00}(\theta, \phi)|^2 (2)(2\pi) \Rightarrow Y_{00}(\theta, \phi) = \frac{1}{\sqrt{4\pi}}$, so no angular dependence in the spherical harmonic.

Now the only contribution is from the radial component:

$$\langle r^2 \rangle_{0,0} = \int_0^\infty r^4 |R_{0,0}(r)|^2 dr.$$

Define $u_{0,0}(r) \equiv rR_{0,0}(r)$, then $R_{0,0}(r) = \frac{u_{0,0}(r)}{r}$. Making the substitution yields

$$\langle r^2 \rangle_{0,0} = \int_0^\infty r^4 \left| \frac{u_{0,0}(r)}{r} \right|^2 dr = \int_0^\infty r^2 |u_{0,0}(r)|^2 dr. \quad 1.1$$

Similarly, by the orthonormality condition on spherical harmonics, we have that

$$\langle r^2 \rangle_{0,1} = \int_0^\infty r^2 |u_{0,1}(r)|^2 dr. \quad 1.2$$

Writing (1.1) and (1.2) in the following ways for simplicity:

$$\langle r^2 \rangle_{0,0} = \int_0^\infty u_{0,0}^2 r^2 dr, \quad A.1$$

$$\langle r^2 \rangle_{0,1} = \int_0^\infty u_{0,1}^2 r^2 dr. \quad A.2$$

To continue the proof, we need to employ the radial form of the Schrödinger equation. We start from the kinetic energy operator in spherical coordinates (Hartree a.u.; equivalent scaled form $\hbar = 2m = 1$) and proceed similarly to how (1.1) and (1.2) were found.

$$\hat{p}^2 = -\nabla^2 = -\frac{1}{r^2} \left[\frac{\partial}{\partial r} \left(r^2 \frac{\partial}{\partial r} \right) - \hat{L}^2 \right]. \quad (\text{Appendix A.2})$$

The spherical harmonics satisfy

$$\hat{L}^2 Y_{\ell m}(\theta, \phi) \equiv \left\{ -\frac{1}{\sin^2 \theta} \left[\sin \theta \frac{\partial}{\partial \theta} \left(\sin \theta \frac{\partial}{\partial \theta} \right) + \frac{\partial^2}{\partial \phi^2} \right] \right\} Y_{\ell m}(\theta, \phi) = \ell(\ell+1) Y_{\ell m}(\theta, \phi). \quad (\text{Appendix A.3})$$

Substituting this into the Schrödinger equation yields a 1-D eigenvalue equation:

$$\frac{d}{dr} \left(r^2 \frac{dR}{dr} \right) - r^2 [V(r) - E] R = \ell(\ell+1) R. \quad 1.3$$

This equation can be further simplified by using the change of variables given by $u \equiv rR$, giving us the following equalities to substitute in:

$$R = \frac{u}{r}.$$

$$\frac{dR}{dr} = \frac{1}{r} \left(\frac{du}{dr} \right) - \frac{u}{r^2} = \frac{r \left(\frac{du}{dr} \right) - u}{r^2}. \quad (\text{Appendix A.4})$$

$$\frac{d}{dr} \left(r^2 \frac{dR}{dr} \right) = \frac{d}{dr} \left(r^2 \left[\frac{r \left(\frac{du}{dr} \right) - u}{r^2} \right] \right) = \frac{d}{dr} \left(r \left(\frac{du}{dr} \right) - u \right) = r \frac{d^2u}{dr^2} + \frac{du}{dr} - \frac{du}{dr} = r \frac{d^2u}{dr^2}. \quad (\text{Appendix A.5})$$

Now making the substitutions into (1.3), we arrive at the radial equation after a few steps:

$$\begin{aligned} r \frac{d^2u}{dr^2} - r^2 V \left(\frac{u}{r} \right) + r^2 E \left(\frac{u}{r} \right) &= \ell(\ell+1) \left(\frac{u}{r} \right) \\ &= r \frac{d^2u}{dr^2} - rVu + rEu = \frac{\ell(\ell+1)}{r} u \\ &= \frac{d^2u}{dr^2} - Vu + Eu = \frac{\ell(\ell+1)}{r^2} u \end{aligned} \quad (\text{Appendix A.6})$$

$$\Rightarrow \boxed{-\frac{d^2u}{dr^2} + \left[V + \frac{\ell(\ell+1)}{r^2} \right] u = Eu},$$

where $\frac{\ell(\ell+1)}{r^2}$ is the centrifugal barrier term.

$$\xrightarrow{\ell=0} -u''_{0,0} + Vu_{0,0} = E_{0,0}u_{0,0}. \quad \text{A.3}$$

$$\xrightarrow{\ell=1} -u''_{0,1} + \frac{2}{r^2}u_{0,1} + Vu_{0,1} = E_{0,1}u_{0,1}. \quad \text{A.4}$$

To show

$$\frac{d}{dr} \left[\frac{u_{0,1}}{u_{0,0}} \right] > 0 \text{ for } u_{0,0} > 0, \quad 1.4$$

we proceed by first finding the derivative explicitly and then implementing the first-derivative test:

$$\frac{d}{dr} \left[\frac{u_{0,1}}{u_{0,0}} \right] = \frac{u_{0,0}u'_{0,1} - u_{0,1}u'_{0,0}}{u_{0,0}^2}. \quad (\text{Appendix A.7})$$

Since $u_{0,0}^2 > 0$, we focus on the numerator (the Wronskian) and its derivative.

$$W(r) = u_{0,0}u'_{0,1} - u_{0,1}u'_{0,0}. \quad (\text{Appendix A.8})$$

$$\begin{aligned}
W'(r) &= u'_{0,0}u'_{0,1} + u_{0,0}u''_{0,1} - [u'_{0,1}u'_{0,0} + u_{0,1}u''_{0,0}] \\
&= u_{0,0}u''_{0,1} - u_{0,1}u''_{0,0}.
\end{aligned} \tag{Appendix A.9}$$

Solving (A.3) and (A.4) for their second derivative terms and plugging into the Wronskian's derivative yields

$$u''_{0,0} = Vu_{0,0} - E_{0,0}u_{0,0} = (V - E_{0,0})u_{0,0}. \tag{A.3*}$$

$$u''_{0,1} = Vu_{0,1} + \frac{2}{r^2}u_{0,1} - E_{0,1}u_{0,1} = \left(V + \frac{2}{r^2} - E_{0,1}\right)u_{0,1}. \tag{A.4*}$$

$$\begin{aligned}
\Rightarrow W'(r) &= u_{0,0} \left(Vu_{0,1} + \frac{2}{r^2}u_{0,1} - E_{0,1}u_{0,1} \right) - u_{0,1} (Vu_{0,0} - E_{0,0}u_{0,0}) \\
&= u_{0,0}u_{0,1} \left(V + \frac{2}{r^2} - E_{0,1} \right) - u_{0,1}u_{0,0} (V - E_{0,0}) \\
&= u_{0,0}u_{0,1} \left(\frac{2}{r^2} + E_{0,0} - E_{0,1} \right).
\end{aligned}$$

1.5

The $\lim_{r \rightarrow 0} W(r) = 0$ because $u_{0,1}(0) = 0 = u'_{0,1}(0)$ due to the nonzero angular momentum term.

- For small r : The $u_{0,0}u_{0,1}$ factor in (1.5) is positive since $u_{0,0} > 0$ and $u_{0,1} \propto r^2$ when r is near zero. Also, the $\frac{2}{r^2}$ term is quite large and overtakes ΔE for sufficiently small r , so we can say with $\frac{2}{r^2} + E_{0,0} - E_{0,1} > 0$ that $W'(r) > 0$ and $W(r) > 0$.
- For large r : $\frac{2}{r^2}$ is quite small and we can say that $\frac{2}{r^2} + E_{0,0} - E_{0,1} < 0$ (since $E_{0,1} > E_{0,0}$), causing $\lim_{r \rightarrow \infty} W(r) = 0$. Importantly, $W(r)$ does not cross zero due to a counting-nodes argument from Sturm-Liouville theory (zero for the (0,0) state; one for the (0,1) state).

$\therefore W(r) > 0$ on $(0, \infty) \Rightarrow \frac{d}{dr} \left[\frac{u_{0,1}}{u_{0,0}} \right] > 0$ for $r > 0$ since the numerator and denominator are both positive on the interval.

Next, we want to show that $u_{0,1}^2 - u_{0,0}^2$ has one zero, namely at $r = r_0$. Letting

$$f(r) = \frac{u_{0,1}}{u_{0,0}}, \tag{Appendix A.10}$$

we can rewrite the difference as

$$\begin{aligned} u_{0,1}^2 - u_{0,0}^2 &= (f(r)u_{0,0})^2 - u_{0,0}^2 \\ &= u_{0,0}^2 (f(r)^2 - 1). \end{aligned} \quad (\text{Appendix A.11})$$

We know that $u_{0,0}^2 > 0$ for $r > 0$, so we will focus on $f(r)^2 - 1$. From (1.4)'s monotonic behavior, we know $f(r) > 0$ on $(0, \infty)$, so $f(r)^2 > 0$ on the same interval. We also know that $f(0) = 0 = f(0)^2$ and proceed with the analysis at the boundaries again:

- For small r : $f(0)^2 - 1 = (0)^2 - 1 = -1 < 0$.
- For large r : Since $u_{0,1}$ decays more slowly than $u_{0,0}$, we can say that $\lim_{r \rightarrow \infty} f(r)^2 > 1 \Rightarrow \lim_{r \rightarrow \infty} f(r)^2 - 1 > 0$. Note that one could also use an asymptotic method for second-order ODEs to show this, like the WKB approximation.

$\therefore u_{0,1}^2 - u_{0,0}^2$ vanishes once on $(0, \infty)$.

Using this result from monotonicity, we can write the difference of the left-hand side's expectation values as an inequality using (A.1) and (A.2):

$$\langle r^2 \rangle_{0,1} - \langle r^2 \rangle_{0,0} = \int_0^\infty (u_{0,1}^2 - u_{0,0}^2)(r^2 - r_0^2) dr > 0. \quad \text{A.5}$$

$$\Rightarrow \langle r^2 \rangle_{0,1} - \langle r^2 \rangle_{0,0} > 0 \Rightarrow \langle r^2 \rangle_{0,0} < \langle r^2 \rangle_{0,1}. \quad (\text{Appendix A.12})$$

Proof. (Right-Hand Side)

We want to show that the following equation is strictly positive:

$$\langle r^2 \rangle_{1,0} - \langle r^2 \rangle_{0,1} = \int_0^\infty r^2 (u_{1,0}^2 - u_{0,1}^2) dr. \quad \text{A.6}$$

Applying the virial theorem (generally $2\langle T \rangle = \langle \vec{r} \cdot \nabla V \rangle$, where $\vec{r} \cdot \nabla V = r \frac{dV}{dr}$ in our 1-D radial equation treatment), we use the normalization of the wavefunctions

$$\int_0^\infty u_{1,0}^2 dr = 1 \quad \text{and} \quad \int_0^\infty u_{0,1}^2 dr = 1 \quad (\text{Appendix A.13})$$

$$\Rightarrow \int_0^\infty (u_{1,0}^2 - u_{0,1}^2) dr = 1 - 1 = 0. \quad \text{A.8}$$

along with integration by parts to show

$$\int_0^\infty (u_{1,0}^2 - u_{0,1}^2) \left[V + \frac{1}{2} r \frac{dV}{dr} \right] dr > 0. \quad \text{A.7}$$

Multiplying (A.3) modified for the $(1, 0)$ state by $u_{1,0}$ and integrating gives

$$\int_0^\infty u_{1,0} \left[-u_{1,0}'' + V u_{1,0} \right] dr = \int_0^\infty E_{1,0} u_{1,0}^2 dr = E_{1,0}(1) = E_{1,0}. \quad 1.6$$

Multiplying (A.4) by $-u_{0,1}$ and integrating over $r \in (0, \infty)$ gives

$$-\int_0^\infty u_{0,1} \left[-u_{0,1}'' + \frac{2}{r^2} u_{0,1} + V u_{0,1} \right] dr = -\int_0^\infty E_{0,1} u_{0,1}^2 dr = -E_{0,1}(1) = -E_{0,1}. \quad 1.7$$

Adding (1.6) and (1.7) yields

$$\int_0^\infty u_{1,0} \left[-u_{1,0}'' + V u_{1,0} \right] dr - \int_0^\infty u_{0,1} \left[-u_{0,1}'' + \frac{2}{r^2} u_{0,1} + V u_{0,1} \right] dr = E_{1,0} - E_{0,1}. \quad 1.8$$

- For the $(1, 0)$ state: First, we look at the term without the potential energy.

$$-\int_0^\infty u_{1,0} u_{1,0}'' dr = -\left(u_{1,0} u_{1,0}' \Big|_0^\infty - \int_0^\infty (u_{1,0}')^2 dr \right) = \int_0^\infty (u_{1,0}')^2 dr \quad (\text{Appendix A.14})$$

because the term $u_{1,0} u_{1,0}' \Big|_0^\infty$ vanishes at the boundaries by $\lim_{r \rightarrow \infty} u_{1,0}(r) = 0$ due to normalization of the wavefunction and $u_{1,0}'(0) \approx 0$ since $u_{1,0}(0)$ is constant.

Next, we look at the potential energy term:

$$\int_0^\infty u_{1,0} V u_{1,0} dr = \int_0^\infty V u_{1,0}^2 dr. \quad (\text{Appendix A.15})$$

- For the $(0, 1)$ state: We proceed in the same manner as for the $(1, 0)$ state:

$$\int_0^\infty u_{0,1} u_{0,1}'' dr = u_{0,1} u_{0,1}' \Big|_0^\infty - \int_0^\infty (u_{0,1}')^2 dr = -\int_0^\infty (u_{0,1}')^2 dr \quad (\text{Appendix A.16})$$

where the term $u_{0,1} u_{0,1}' \Big|_0^\infty$ vanishes at ∞ for the same reason as the $(0, 0)$ state but vanishes at 0 because $u_{0,1}(0) = 0$ due to $\ell = 1$ as previously described.

Looking at the potential energy terms, we have

$$-\int_0^\infty u_{0,1} V u_{0,1} dr = -\int_0^\infty V u_{0,1}^2 dr, \quad (\text{Appendix A.17})$$

$$-\int_0^\infty u_{0,1} \left[\frac{2}{r^2} u_{0,1} \right] dr = -\int_0^\infty \frac{2}{r^2} u_{0,1}^2 dr. \quad (\text{Appendix A.18})$$

- Combining the two states: Plugging these integrals into (1.8) gives us

$$\int_0^\infty \left((u'_{1,0})^2 - (u'_{0,1})^2 \right) dr + \int_0^\infty V (u_{1,0}^2 - u_{0,1}^2) dr - \int_0^\infty \frac{2}{r^2} u_{0,1}^2 dr = E_{1,0} - E_{0,1} \quad 1.9$$

Finally, to show that (A.7) is strictly positive, we will use the virial theorem to relate the potential with its derivative:

$$E_{1,0} = \int_0^\infty V u_{1,0}^2 dr + \frac{1}{2} \int_0^\infty r V' u_{1,0}^2 dr,$$

$$E_{0,1} = \int_0^\infty V u_{0,1}^2 dr + \frac{1}{2} \int_0^\infty r V' u_{0,1}^2 dr + \int_0^\infty \frac{u_{0,1}^2}{r^2} dr.$$

Subtracting these equations:

$$\int_0^\infty (u_{1,0}^2 - u_{0,1}^2) \left(V + \frac{1}{2} r V' \right) dr = E_{1,0} - E_{0,1} + \int_0^\infty \frac{u_{0,1}^2}{r^2} dr.$$

We know from condition (A) that $E_{1,0} > E_{0,1}$ due to $V(r)$ being monotonically increasing, so wavefunctions forced outward by higher angular momentum (e.g., the $(0, 1)$ state) end up with lower total energy (can also show with a Sturm-Liouville argument as before). This condition and the fact that the centrifugal barrier term is positive allow us to claim that Eq. (A.7) is strictly positive.

Combining this result with the monotonicity of the r^2 factor in (A.6), it follows that

$$\langle r^2 \rangle_{1,0} - \langle r^2 \rangle_{0,1} > 0 \Rightarrow \langle r^2 \rangle_{0,1} < \langle r^2 \rangle_{1,0}.$$

By the transitivity of the chain of inequalities, we have shown that

$$\langle r^2 \rangle_{0,0} < \langle r^2 \rangle_{0,1} < \langle r^2 \rangle_{1,0}. \quad \square$$

A.2. Upper Bound for 2nd Moment of Position of Ground State

Theorem Appendix A.2.

$$\langle r^2 \rangle_{0,0} \leq \frac{3}{m(E_{0,1} - E_{0,0})},$$

where m is the common mass of the quark-antiquark system, or, in the general case, 2 times the reduced mass.

Proof.

$$\begin{aligned}
& \langle 0, 0 | [\hat{H}, \hat{x}] \hat{x} | 0, 0 \rangle \\
&= \sum_n \langle 0, 0 | [\hat{H}, \hat{x}] | n \rangle \langle n | \hat{x} | 0, 0 \rangle && \text{(since } \sum_n |n\rangle \langle n| = \mathbb{1}\text{)} \\
&= \sum_n \langle 0, 0 | \hat{H} \hat{x} - \hat{x} \hat{H} | n \rangle \langle n | \hat{x} | 0, 0 \rangle \\
&= \sum_n \left(\langle 0, 0 | \hat{H} \hat{x} | n \rangle - \langle 0, 0 | \hat{x} \hat{H} | n \rangle \right) \langle n | \hat{x} | 0, 0 \rangle \\
&= \sum_n (E_{0,0} \langle 0, 0 | \hat{x} | n \rangle - E_n \langle 0, 0 | \hat{x} | n \rangle) \langle n | \hat{x} | 0, 0 \rangle && \text{A.13} \\
&= \sum_n (E_{0,0} - E_n) \langle 0, 0 | \hat{x} | n \rangle \langle n | \hat{x} | 0, 0 \rangle \\
&= \sum_n (E_{0,0} - E_n) \langle n | \hat{x} | 0, 0 \rangle^* \langle n | \hat{x} | 0, 0 \rangle \\
&= \sum_n (E_{0,0} - E_n) |\langle n | \hat{x} | 0, 0 \rangle|^2.
\end{aligned}$$

Evaluating with test function $f(x)$, we have:

$$\begin{aligned}
[\hat{H}, \hat{x}] f(x) &= \frac{1}{2m} [\hat{p}_x^2, \hat{x}] f(x) = \frac{1}{2m} [(-i\nabla_x)^2, \hat{x}] f(x) \\
&= \frac{1}{2m} \left[\frac{-\partial^2}{\partial x^2}, \hat{x} \right] f(x) \\
&= \frac{1}{2m} \left(\frac{-\partial^2}{\partial x^2} (x f(x)) - x \left(\frac{-\partial^2}{\partial x^2} f(x) \right) \right) \\
&= \frac{1}{2m} \left(\frac{-\partial}{\partial x} (f(x) + x f'(x)) + x f''(x) \right) && \text{II} \\
&= \frac{1}{2m} \left(-(f'(x) + f'(x) + x f''(x)) + x f''(x) \right) \\
&= \frac{1}{2m} (-2f'(x)) = \frac{-1}{m} f'(x). \\
&\Rightarrow [\hat{H}, \hat{x}] = \frac{-1}{m} \frac{\partial}{\partial x}.
\end{aligned}$$

$$\begin{aligned}
[\hat{H}, \hat{x}] \hat{x} &= \frac{-1}{m} \frac{\partial}{\partial x} (x) = \frac{-1}{m}. \\
&\Rightarrow \langle 0, 0 | [\hat{H}, \hat{x}] \hat{x} | 0, 0 \rangle = \langle 0, 0 | -\frac{1}{m} | 0, 0 \rangle && \text{III} \\
&= -\frac{1}{m} \langle 0, 0 | 0, 0 \rangle = -\frac{1}{m}.
\end{aligned}$$

Equating (A.13) and (III) gives

$$\sum_n (E_{0,0} - E_n) |\langle n | \hat{x} | 0, 0 \rangle|^2 = \frac{-1}{m}. \quad \text{(Appendix A.19)}$$

$$\Rightarrow (E_{0,0} - E_{0,1}) |\langle n | \hat{x} | 0, 0 \rangle|^2 \leq -\frac{1}{m}, \quad \text{since the } (0, 1) \text{ state is the lowest intermediate } n \text{ state.}$$

(Appendix A.20)

$$\Rightarrow (E_{0,1} - E_{0,0}) |\langle n | \hat{x} | 0, 0 \rangle|^2 \leq \frac{1}{m}. \quad \text{A.14}$$

Using $r^2 = x^2 + y^2 + z^2$, then by symmetry, we have:

$$(E_{0,1} - E_{0,0}) |\langle n | \hat{r} | 0, 0 \rangle|^2 \leq \frac{3}{m}$$

$$|\langle n | \hat{r} | 0, 0 \rangle|^2 \leq \frac{3}{m(E_{0,1} - E_{0,0})}. \quad \text{(Appendix A.21)}$$

Therefore,

$$\langle r^2 \rangle_{0,0} \leq \frac{3}{m(E_{0,1} - E_{0,0})}. \quad \text{A.15}$$

Note that if using the general case mentioned in the theorem, we could write the result as:

$$\langle r^2 \rangle_{0,0} \leq \frac{3}{2\mu(E_{0,1} - E_{0,0})}. \quad \text{(Appendix A.22)}$$

A.3. Bounds for 2nd Moment of Position of the (0, 1) State

Theorem Appendix A.3.

$$\frac{2}{m(E_{0,1} - E_{0,0})} \leq \langle r^2 \rangle_{0,1} \leq \frac{3 + (E_{1,0} - E_{0,0}) / (E_{0,1} - E_{0,0})}{m(E_{1,0} - E_{0,1})}.$$

Here, the inequality is given for the case $E_{0,1} < E_{1,0} < E_{0,2}$, for which conditions (A) and (B) are sufficient.

Proof.

Right-hand side. We start with the (0, 1) state in 1-D (oriented along the x-axis) and consider (known from Theorem 2's proof)

$$\sum_n (E_n - E_{0,1}) |\langle n | \hat{x} | 0, 1_x \rangle|^2 = \frac{1}{m}, \quad \text{A.16}$$

i.e.,

$$\sum_{E_n > E_{0,1}} (E_n - E_{0,1}) |\langle n | \hat{x} | 0, 1_x \rangle|^2 + (E_{0,0} - E_{0,1}) |\langle 0, 0 | \hat{x} | 0, 1_x \rangle|^2 = \frac{1}{m}$$

$$\Rightarrow \sum_{E_n > E_{0,1}} (E_n - E_{0,1}) |\langle n | \hat{x} | 0, 1_x \rangle|^2 = \frac{1}{m} + (E_{0,1} - E_{0,0}) |\langle 0, 0 | \hat{x} | 0, 1_x \rangle|^2,$$

(Appendix A.23)

and so

$$[\inf(E_{1,0} - E_{0,1}, E_{0,2} - E_{0,1})] \sum |\langle n|\hat{x}|0, 1_x\rangle|^2 \leq \frac{1}{m} \left[2 + \frac{\inf(E_{1,0} - E_{0,1}, E_{0,2} - E_{0,1})}{E_{0,1} - E_{0,0}} \right]. \quad \text{A.17}$$

We have an equation for the y operator given as

$$\sum_{E_n \geq E_{0,2}} (E_n - E_{0,1}) |\langle n|\hat{y}|0, 1_x\rangle|^2 = \frac{1}{m}, \quad \text{A.18}$$

Remark Appendix A.3 (Justification of (A.17)–(A.18) and the \hat{z} analogue). The double-commutator (Thomas–Reiche–Kuhn) sum rule gives, for any Cartesian component $q \in \{x, y, z\}$,

$$\sum_n (E_n - E_{0,1}) |\langle n|\hat{q}|0, 1_x\rangle|^2 = \frac{1}{m}, \quad (\text{Appendix A.24})$$

consistent with (A.16). Decomposing the x -sum into the ground-state piece and the rest,

$$\sum_{E_n > E_{0,1}} (E_n - E_{0,1}) |\langle n|\hat{x}|0, 1_x\rangle|^2 = \frac{1}{m} + (E_{0,1} - E_{0,0}) |\langle 0, 0|\hat{x}|0, 1_x\rangle|^2,$$

and bounding from below with the smallest accessible excitation gap $\Delta_{\min}^{(x)} := \inf(E_{1,0} - E_{0,1}, E_{0,2} - E_{0,1})$ yields (A.17) after division by $\Delta_{\min}^{(x)}$.

For y and z , the same TRK identity holds:

$$\sum_n (E_n - E_{0,1}) |\langle n|\hat{y}|0, 1_x\rangle|^2 = \frac{1}{m}, \quad \sum_n (E_n - E_{0,1}) |\langle n|\hat{z}|0, 1_x\rangle|^2 = \frac{1}{m}. \quad (\text{Appendix A.25})$$

By dipole ($E1$) selection rules, \hat{y} and \hat{z} connect $(0, 1)_x$ only to states with $\Delta\ell = \pm 1$ and suitable m ; in particular, the $(0, 0)$ term vanishes for \hat{y}, \hat{z} in this orientation, so the minimal excitation is $E_{0,2} - E_{0,1}$. Thus,

$$\sum_{E_n \geq E_{0,2}} (E_n - E_{0,1}) |\langle n|\hat{z}|0, 1_x\rangle|^2 = \frac{1}{m},$$

which justifies (A.18) and its \hat{z} counterpart. Combining the x, y, z bounds and applying (\star) – (\dagger) then yields (A.19).

$$m\langle r^2 \rangle_{0,1} \leq \frac{2}{E_{0,2} - E_{0,1}} + \frac{1}{E_{0,1} - E_{0,0}} + \frac{2}{\inf(E_{1,0} - E_{0,1}, E_{0,2} - E_{0,1})}. \quad \text{A.19}$$

Dividing both sides by m and applying (†) to the first term on the right-hand side of (A.19) and (★) to the third term gives

$$\begin{aligned} \langle r^2 \rangle_{0,1} &\leq \frac{1}{m} \left[\frac{2}{E_{1,0} - E_{0,1}} + \frac{1}{E_{0,1} - E_{0,0}} + \frac{2}{E_{1,0} - E_{0,1}} \right] \\ &= \frac{1}{m} \left[\frac{4}{E_{1,0} - E_{0,1}} + \frac{1}{E_{0,1} - E_{0,0}} \right] \\ &= \frac{1}{m(E_{1,0} - E_{0,1})} \left[3 + \frac{E_{1,0} - E_{0,0}}{E_{0,1} - E_{0,0}} \right], \end{aligned} \tag{Appendix A.26}$$

which matches the RHS bound in the theorem.

Left-hand side. Applying Cauchy–Schwarz to $f = r u_{0,1}$ and $g = u_{0,0}$ gives

$$\int_0^\infty r^2 u_{0,1}^2 dr \geq \left(\int_0^\infty r u_{0,0} u_{0,1} dr \right)^2. \tag{A.20}$$

Next, multiply the (0,0)- and (0,1)-channel radial Schrödinger equations by $u_{0,1}$ and $u_{0,0}$, respectively, subtract, and integrate by parts; in Hartree a.u. (equivalently, after rescaling the $\hbar = 2m = 1$ form), this yields

$$(E_{0,1} - E_{0,0}) \int_0^\infty r u_{0,0} u_{0,1} dr = 2 \int_0^\infty u'_{0,0} u_{0,1} dr. \tag{A.22}$$

A further Cauchy–Schwarz estimate gives

$$2 \left| \int_0^\infty u'_{0,0} u_{0,1} dr \right| \leq 2 \|u'_{0,0}\|_2 \|u_{0,1}\|_2 = 2 \|u'_{0,0}\|_2. \tag{A.23}$$

Combining (A.20)–(A.23), together with the standard Hardy inequality for $\ell = 0$ channels,

$$\int_0^\infty \frac{u_{0,0}^2}{r^2} dr \leq 4 \int_0^\infty (u'_{0,0})^2 dr,$$

one arrives at

$$\langle r^2 \rangle_{0,1} \geq \frac{2}{E_{0,1} - E_{0,0}}, \tag{A.24}$$

which is the claimed left-hand inequality. \square

Appendix B

Interpolation methods.

Why the Bertlmann–Martin inequalities do not deliver odd moments.

Let $\mu_n := \langle r^n \rangle = \int_0^\infty r^n \rho(r) 4\pi r^2 dr$ denote ground–state radial moments (with $\rho(r) \geq 0$ and $r = |\mathbf{r}|$). In general $\mu_{2k+1} > 0$ (e.g., $\langle r \rangle > 0$); so the issue is *not* vanishing odd moments. The point is structural: the Bertlmann–Martin (BM) framework builds bounds and recurrences from positivity of energy–weighted spectral

sums involving multipole operators $Q_{\ell m} = r^\ell Y_{\ell m}(\hat{\mathbf{r}})$ and nested commutators with H . After the angular sums, one obtains scalar constraints that couple *even* multipole ranks—hence even powers of r . Concretely, the BMI-type recursions link μ_{2k} to μ_{2k-2} (and spectral data), but contain no terms that connect to μ_{2k+1} . Thus BMIs propagate only the even subsequence $\{\mu_0, \mu_2, \mu_4, \dots\}$; the odd subsequence $\{\mu_1, \mu_3, \dots\}$ is left undetermined and must be supplied by an auxiliary ansatz or interpolation.

Why Padé approximants are needed beyond q_{\max} . When $L(q)$ is built from finitely many moments,

$$L(q) = \sum_{n=0}^N a_n q^n + \mathcal{O}(q^{N+1}), \quad a_n = (-1)^n \mu_n / n!,$$

the resulting power series is a local representation about $q = 0$ with a finite radius of convergence R , set by the nearest complex- q singularity (poles/branch points associated with excitation thresholds, continuum onset, etc.). Accurate inversion kernels (Bromwich, Talbot, Euler) and the recovery of short-range structure in $\chi^2(r)$ require reliable values of $L(q)$ for q extending past the moment-limited $q_{\max} \leq R$. Truncated Taylor series degrade rapidly near the convergence boundary and are unusable for $q > R$. A Padé approximant $[L/M](q) = P_L(q)/Q_M(q)$ matches the known series coefficients up to order $L + M$ while providing a rational *analytic continuation* that (i) remains accurate closer to and often beyond the circle of convergence, and (ii) can mimic true singularity structure via poles/zeros. This continuation is what makes the numerical inverse stable and accurate when the integral requires q -values beyond the safe Taylor regime; hence Padé is generally necessary to push past q_{\max} and recover r -space features without severe bias or instability.

Appendix C

C.1. Overview

The Roehrl-style Least Squares (LSQ) approach [21,22,23] provides a variational baseline algorithm for reconstructing the potential $q(x)$ in the one-dimensional Sturm–Liouville equation

$$-u''(x) + q(x)u(x) = \lambda u(x), \quad x \in [0, 1], \quad (\text{Appendix C.1})$$

from two spectra corresponding to different separated boundary conditions. Let (α, β) and (α, γ) denote two sets of boundary angles, with $\sin(\beta - \gamma) \neq 0$, and let $\lambda_{q,i,n}$ be the n -th eigenvalue for boundary condition set $i \in \{1, 2\}$. Borg’s and Levinson’s theorems guarantee uniqueness of $q(x)$ given the full two spectra.

C.2. Least Squares Functional

Given partial spectral data $\{\lambda_{Q,i,n}\}_{(i,n)\in I}$ of an unknown potential $Q(x)$, the LSQ method minimizes the functional

$$G[q] = \sum_{(i,n)\in I} \omega_{i,n} (\lambda_{q,i,n} - \lambda_{Q,i,n})^2, \quad (\text{Appendix C.2})$$

where $\omega_{i,n} > 0$ are user-defined weights (often $\omega_{i,n} = 1$). The functional satisfies $G[q] \geq 0$ and $G[q] = 0$ if and only if $\lambda_{q,i,n} = \lambda_{Q,i,n}$ for all $(i,n) \in I$.

C.3. Gradient and Convexity

Let $g_{q,i,n}(x)$ denote the normalized eigenfunction corresponding to $\lambda_{q,i,n}$. The Fréchet derivative of the eigenvalue in direction $h(x)$ is

$$\frac{\partial}{\partial q} \lambda_{q,i,n}[h] = \int_0^1 h(x) g_{q,i,n}^2(x) dx. \quad (\text{Appendix C.3})$$

Thus, the gradient of G is

$$\nabla G[q](x) = 2 \sum_{(i,n)\in I} \omega_{i,n} (\lambda_{q,i,n} - \lambda_{Q,i,n}) g_{q,i,n}^2(x). \quad (\text{Appendix C.4})$$

The squared eigenfunctions $\{g_{q,i,n}^2\}$ are linearly independent in $H^1[0,1]$, implying that $\nabla G[q] = 0$ if and only if $G[q] = 0$ in the idealized formulation. This supports gradient-based minimization as a principled baseline, while finite-grid and finite-data implementations still require empirical convergence checks and sensitivity audits.

C.4. Numerical Minimization

In practice, $G[q]$ is minimized using the Polak–Ribière conjugate gradient algorithm. The iterative process is:

- (1) Initialize with a trial potential $q^{(0)}(x)$ (often $q^{(0)} \equiv 0$).
- (2) At iteration k :
 - (a) Compute eigenvalues and eigenfunctions for both boundary condition sets.
 - (b) Evaluate $G[q^{(k)}]$ and $\nabla G[q^{(k)}]$ via Eq. (Appendix C.4).
 - (c) Determine a search direction using conjugate gradients.
 - (d) Perform a line search to find the optimal step length α_k .
 - (e) Update $q^{(k+1)} = q^{(k)} + \alpha_k d_k$.

This procedure continues until $G[q]$ falls below a set tolerance or a maximum iteration count is reached.

C.5. Implementation in the Benchmark Script

In the benchmarking framework, the LSQ functional (Appendix C.2) is implemented using:

- Discrete grid representation of $q(x)$.
- Finite-difference assembly of the discrete Sturm–Liouville operator for Dirichlet–Dirichlet and Dirichlet–Neumann boundary conditions.
- Direct diagonalization to obtain $\lambda_{q,i,n}$ and $g_{q,i,n}$.
- Gradient evaluation according to Eq. (Appendix C.4).
- Optional regularization term $\mu \int (q'(x))^2 dx$ for smoothing.

The Polak–Ribière conjugate gradient loop uses an Armijo line search to ensure descent and numerical stability.

C.6. Role as a Benchmark

This LSQ method is used as a reference baseline against the Laplace-transform-based inverse method developed in this work. Unlike the Laplace approach, which reconstructs $q(x)$ from ground-state density moments (enforced to satisfy Bertlmann–Martin inequalities), the LSQ method directly fits the spectral data in a two-spectra setting. It is therefore useful as a benchmark because:

- (1) In the ideal two-spectra setting, it targets the exact potential through direct spectral-misfit minimization.
- (2) It provides a complementary reconstruction family with different assumptions and failure modes than the Laplace/GBM pipeline.
- (3) It makes no assumptions about moment sequences or analytic continuation.

In the full comparison pass, the LSQ method serves as a reproducible reference baseline; comparative conclusions are drawn from reported metrics and figures for the specific benchmark settings documented for this draft. For benchmark-count comparisons, LSQ is treated as 120 total constraints (60 DD + 60 DN), while Laplace/GBM counts use recurrence-consumed inputs rather than `levels_spec`.

C.7. Further Benchmark Figures

For the Coulomb potential:

Table Appendix C.1. Benchmark comparison between Röhrl-style LSQ and Laplace Method for Coulomb potential.

Metric	Röhrl-style LSQ	Laplace Method
Iterations	300	–
Elapsed time (s)	5.422071e+01	1.259797e+01
L2 ($q_{\text{rec}}, q_{\text{true}}$)	6.417976e-04	9.586654e-04
RMSE eigenvalues (DD)	2.543589e-05	2.019329e-04
RMSE eigenvalues (DN)	3.594460e-05	2.016194e-04
Final F	4.910380e-10	–
Final eig. misfit (both sets)	8.703796e-05	2.553403e-04

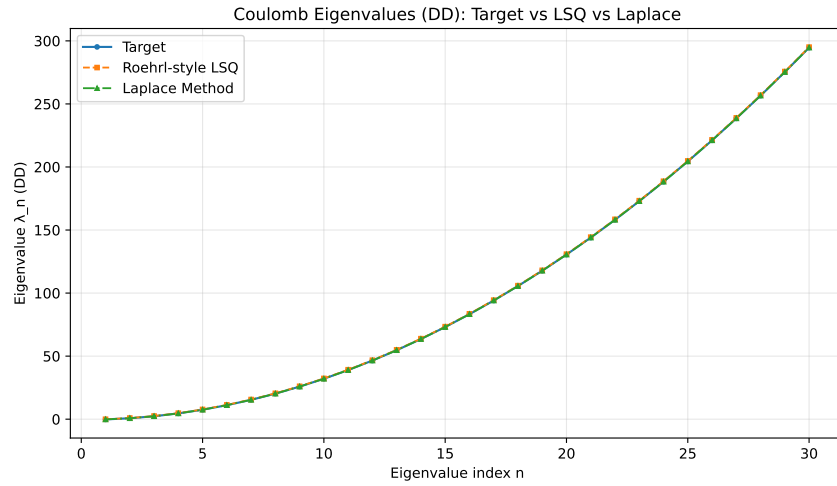


Fig. Appendix C.1. Fit for eigenvalues using the Dirichlet-Dirichlet boundary conditions.

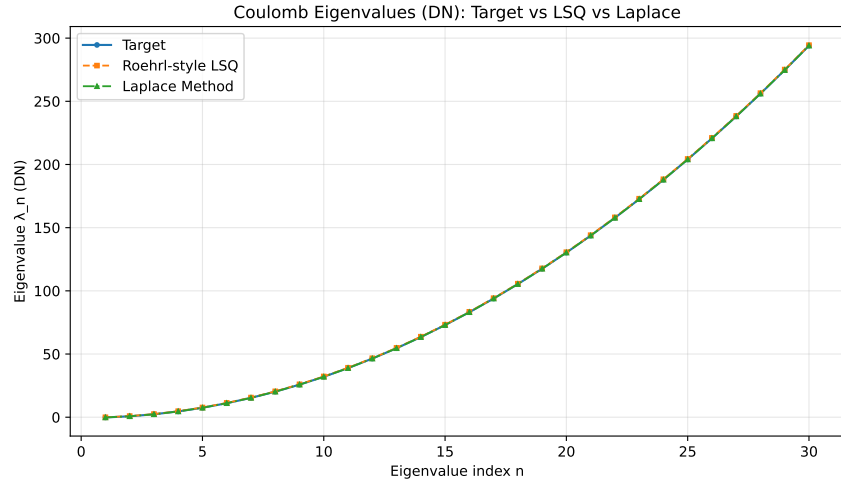


Fig. Appendix C.2. Fit for eigenvalues using the Dirichlet-Neumann boundary conditions.

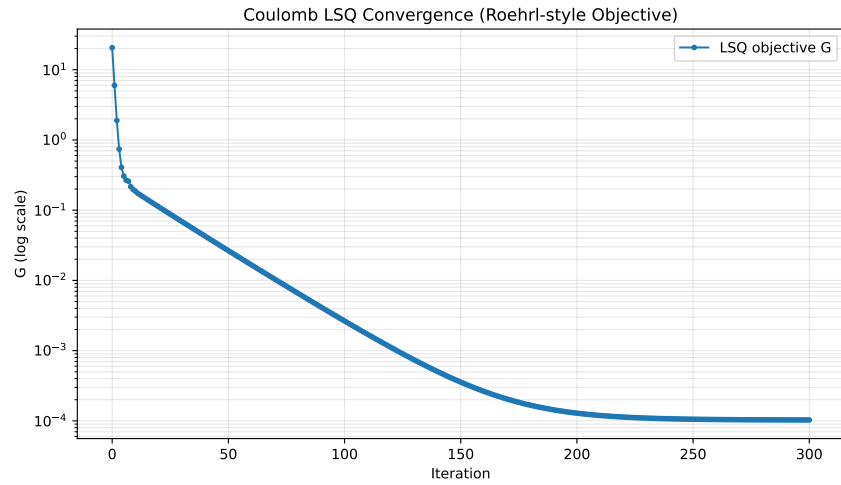


Fig. Appendix C.3. Least-squares (LSQ) convergence for Roehrl’s two-spectra inverse Sturm–Liouville functional. The curve plots the objective $F(c) = G(c) + \mu R(c)$ versus nonlinear conjugate-gradient (Polak–Ribière) iteration. Here G is the weighted sum of squared eigenvalue mismatches for the DD and DN problems, and R is an optional smoothing penalty on q' .

References

- [1] V. Ambarzumian, Über eine frage der eigenwerttheorie, *Zeitschrift für Physik* **53**(9-10) (1929) 690–695.
- [2] G. Borg, Eine umkehrung der sturm-liouvilleschen eigenwertaufgabe: Bestimmung der differentialgleichung durch die eigenwerte, *Acta Mathematica* **78** (1946) 1–96.
- [3] N. Levinson, The inverse Sturm-Liouville problem, *Matematisk Tidsskrift B* **1949** (1949) 25–30.
- [4] A. N. Tikhonov, Über die eindeutigkeit der lösung des problems der elektro-schürfung, *Doklady Akademii Nauk SSSR, Novaya Seriya* **69** (1949) 797–800.
- [5] I. M. Gel’fand and B. M. Levitan, On the determination of a differential equation from its spectral function, *American Mathematical Society Translations, Series 2* **1** (1955) 253–304.
- [6] V. A. Marchenko, Some questions of the theory of homogeneous linear differential operators of the second order. i, ii Tr. Mosk. Mat. Obshch. 1, 327–420 (1952); 2, 4–82 (1953), (1953).
- [7] B. D. Lowe, M. Pilant and W. Rundell, The recovery of potentials from finite spectral data, *SIAM Journal on Mathematical Analysis* **23**(2) (1992) 482–504.
- [8] J. R. McLaughlin and G. H. Handelman, Sturm-liouville inverse eigenvalue problems *Mechanics Today*, Vol. 5, pp. 281–295, (1980).
- [9] P. E. Sacks, An iterative method for the inverse dirichlet problem, *Inverse Problems* **4**(4) (1988) 1055–1069.
- [10] W. Rundell and P. E. Sacks, Reconstruction techniques for classical inverse Sturm-Liouville problems, *Mathematics of Computation* **58**(197) (1992) 161–183.
- [11] O. H. Hald, The inverse Sturm-Liouville problem with symmetric potentials, *Acta Mathematica* **141** (1978) 263–291.
- [12] V. V. Kravchenko, On a method for solving the inverse Sturm-Liouville problem, *Journal of Inverse and Ill-Posed Problems* **27**(3) (2019) 401–407.
- [13] K. Chadan and P. C. Sabatier, *Inverse Problems in Quantum Scattering Theory* (Springer, 2012).
- [14] R. G. Newton, *Scattering Theory of Waves and Particles*, 2 edn. (Springer, 2013).
- [15] A. G. Ramm and S. Gutman, Optimization methods in direct and inverse scattering In *Continuous Optimization: Current Trends and Modern Applications* (Applied Optimization), pp. 51–110, Springer, (2005).
- [16] R. Yekken, F.-Z. Ighezou and R. J. Lombard, The inverse problem in the case of bound states, *Annals of Physics* **323**(1) (2008) 61–81.
- [17] R. Mezhoud, I. Ami and R. J. Lombard, The use of laplace transform in the inverse problem from bound states, *Romanian Reports in Physics* **75**(3) (2023) 114–114.
- [18] R. A. Bertlmann and A. Martin, Inequalities on heavy quark–antiquark systems, *Nuclear Physics B* **168** (1980) 111–136.
- [19] V. V. Kravchenko, Reconstruction techniques for complex potentials, *Journal of Mathematical Physics* **65**(3) (2024) p. 033501.
- [20] Wikipedia contributors, Stieltjes transformation — wikipedia, the free encyclopedia (2025), Accessed 2026-02-23.
- [21] N. Röhrl, A least squares functional for solving inverse sturm-liouville problems (2005), arXiv:math/0502407.
- [22] N. Röhrl, Recovering boundary conditions in inverse Sturm-Liouville problems, *Contemporary Mathematics* **412** (2006) 263–270.
- [23] N. Röhrl, A least-squares functional for solving inverse sturm-liouville problems, *Inverse Problems* **21**(6) (2005) 2009–2017.